



LAWRENCE
LIVERMORE
NATIONAL
LABORATORY

Experimental and Numerical Investigations of Beryllium Strength Models Using the Rayleigh-Taylor Instability

M. T. Henry de Frahan, J. L. Belof, R. M. Cavallo,
O. Ignatova, E. Johnson, V. Raevsky, B. A.
Remington

October 16, 2014

Journal of Applied Physics

Disclaimer

This document was prepared as an account of work sponsored by an agency of the United States government. Neither the United States government nor Lawrence Livermore National Security, LLC, nor any of their employees makes any warranty, expressed or implied, or assumes any legal liability or responsibility for the accuracy, completeness, or usefulness of any information, apparatus, product, or process disclosed, or represents that its use would not infringe privately owned rights. Reference herein to any specific commercial product, process, or service by trade name, trademark, manufacturer, or otherwise does not necessarily constitute or imply its endorsement, recommendation, or favoring by the United States government or Lawrence Livermore National Security, LLC. The views and opinions of authors expressed herein do not necessarily state or reflect those of the United States government or Lawrence Livermore National Security, LLC, and shall not be used for advertising or product endorsement purposes.

Experimental and Numerical Investigations of Beryllium Strength Models Using the Rayleigh-Taylor Instability

M. T. Henry de Frahan,^{1,a)} J. L. Belof,² R. M. Cavallo,² O. Ignatova,³ E. Johnsen,¹
V. Raevsky,³ and B. A. Remington²

¹*Mechanical Engineering, University of Michigan, Ann Arbor, Michigan, 48109, USA*

²*Lawrence Livermore National Laboratory Livermore, California 94551-0808, USA*

³*Russian Federal Nuclear Center-VNIIEF, Sarov, Russia*

A recent collaboration between LLNL and VNIIEF has produced a set of high explosive driven Rayleigh-Taylor strength data for beryllium. Design simulations using legacy strength models from Steinberg-Lund and Preston-Tonks-Wallace (PTW) suggested an optimal design that would delineate between not just different strength models, but different parameters sets of the PTW model. Application of the models to the post-shot results, however, shows close to classical growth. We characterize the material properties of the beryllium tested in the experiments. We also discuss recent efforts to simulate the data using the legacy strength models as well as the more recent RING relaxation model developed at VNIIEF. Finally, we present shock and ramp-loading recovery experiments conducted as part of the collaboration.

This work was performed under the auspices of the U.S. Department of Energy by Lawrence Livermore National Laboratory under Contract DE-AC52-07NA27344.

Keywords: Rayleigh-Taylor, beryllium, strength model

I. INTRODUCTION:

Beryllium (Be) is a metal with many excellent structural properties and unique radiation characteristics.¹ It has a high elastic modulus, a low Poisson ratio, a low density, and a high melting point. Be has an elastic stiffness comparable to steel and a quarter the density.² Its high strength to weight ratio and high melting point makes it ideal for many defense and aerospace applications.³⁻⁷ However, its toxicity and its low ductility at room temperature has limited the widespread use of Be.

Early investigations of Be focused primarily on dynamic material properties of polycrystalline Be under tensile stress conditions.⁸ Initial Be equation of state descriptions and shock wave profiles up to 5GPa provided material constants for early analytic models.⁹ Christman and Feistmann¹⁰ also investigated dynamic properties of Be such as elastic constants and elastic precursor decay. The data showed a yield plateau, strain hardening, and strain-rate sensitivity.

^{a)} Author to whom correspondence should be addressed. Electronic mail: marchdf@umich.edu.

Using biaxial tensile tests, Lindholm et al.¹¹ and Lindholm and Yeakley⁸ observed yield, plastic flow, and failure of Be under plane stress conditions. Pope and Johnson¹² performed the first attempt at studying Be yielding on primary slip planes of Be using shock loading planar impact of single crystal Be. They also studied the effects of material anisotropy on plane wave propagation. Deformation mechanisms in Be received increasing attention soon thereafter. Jönsson and Beuers¹³ studied the dislocation microstructure of single crystal Be at 2 % strain. Christian and Mahajan¹⁴ provided an extensive review of twinning in various crystal structures, including Be. Using Split-Hopkinson pressure bar experiments with strain-rates from 10^{-3} to 10^4 s^{-1} , Blumenthal et al.^{1,15} studied the evolution of dynamic mechanical behavior and crystallographic texture to understand deformation mechanisms and the role of texture in polycrystalline Be. Brown et al.¹⁶ showed how active deformation mechanisms can be controlled via manipulation of straining direction,¹⁷ deformation temperature,¹⁸ deformation rate², and crystallographic texture¹⁹. Brown et al.¹⁹ extensively investigated the importance and relative contribution of twinning and slip in Be over a range of strain-rates (10^{-4} to 10^4 s^{-1}). Other experimental data² showed the dominance of twinning at strain-rates around 10^4 s^{-1} .

Be failure modes and spall have been the focus of recent experimental work. Experiments of explosively loaded Be samples up to strain-rates of 10^4 - 10^5 s^{-1} were used to investigate Be spall fracture and showed a weak dependence between the spall strength and strain-rate.²⁰ Adams et al.^{21,22} observed elastic precursor decay as a function of target thickness in plate impactor experiments. In earlier experiments, their data indicated brittle spall behavior and a long rise-time in the elastic and plastic waves, which they attribute to twinning being the predominant initial deformation mechanism.²¹ In another set of plate-impactor experiments, Mescheryakov^{23,24} instigated spallation in the Be sample and showed that the dynamic failure during spallation depends strongly on the plastic instability threshold. Recent experiments^{25,26} used post-mortem analysis of explosively driven Be to evaluate failure behaviors. Peak shock pressures of 15GPa were observed but no definite source of failure in Be was identified.²⁵

Few dynamic studies of Be have been performed in recent years and little is known about its strength properties at high strain, strain-rate, and pressure. Currently, there are many competing material strength models relating the yield stress to the strain, strain-rate, and shear modulus. Most are phenomenological and established using physics-based ansatz equations with multiple parameters that are calibrated using data from experiments in low pressure, strain, and strain-rate regimes, e.g. data from Split-Hopkinson pressure bar experiments (at zero pressure, strains of 10 – 20 %, and rates below 10^4 s^{-1}) or Taylor anvil experiments ($\sim 10 \text{ GPa}$, strains of 0.1²⁷, and rates near 10^5 s^{-1}). Because the models are typically tied to phenomenology,

they tend to diverge when confronted with data far from their calibration points, whether that is in pressure, strain or strain-rate space, Figure 1. These data-sparse regimes are particularly of interest to inertial confinement fusion and extreme material loading experiments. In this paper, we discuss a set of dynamic experiments to characterize Beryllium (Be) strength and discriminate among different strength models by providing data in these regimes.

The Rayleigh-Taylor (RT) instability occurs at the interface between two materials accelerated such that the pressure and density gradients are anti-parallel.^{28,29} Under conditions where the accelerated material has no strength (and low viscosity) a surface perturbation grows non-linearly as t^2 , where t is time. However, in the instances where the material remains solid, the perturbation growth is mitigated and even halted depending on the mode of the interface perturbation.³⁰ In 1974 Barnes et al.³¹ took advantage of this observation and developed a technique to accelerate aluminum and stainless steel plates that had surface perturbations using high explosives (HE). By setting off an HE charge at a stand-off distance of $\sim 1.3 - 2.5$ cm, they accelerated the plates without shocking the material and reached peak pressures of 10 GPa. By modeling the growth of imposed sinusoidal perturbations on the side of the material facing the expanding HE products they inferred the influence of strength during the dynamic loading process. Others have since expanded the technique to other materials using modern diagnostic techniques, as well as traditional flash radiography.^{32,33} We designed HE-driven RT experiments for quasi-isentropic loading of Be to reach pressures of 50 GPa and strain-rates of 10^6 s⁻¹. These are pressure and strain-rate regimes where data are sparse and strength models diverge in their predicted behavior.

This article is organized as follows. We describe the setup of the high-explosive (HE)-driven Rayleigh-Taylor (RT) experiments and present the experimental results in Section II. After discussing the existing strength models we compare the experimental results to simulations of the experiments in Section III. We end with a discussion of Be recovery experiments.

II. Experiments

A. Rayleigh-Taylor Experimental Design

The experimental setup is shown in Figure 2. A two stage planar HE drive launches an iron impactor at a second charge of HE, overdriving it beyond the Chapman-Jouguet pressure. The detonated HE expands across the vacuum gap and loads the Be target, which has a machined surface perturbation at the loaded surface, Figure 3, with a quasi-isentropic compression wave, thereby initiating a RT instability at the HE-Be interface. A plexiglass bracket initially holds the Be target in place before the target is accelerated by the HE. The Be targets are made of S200F Be composed of 98.5% pure Be with a maximum of 1.5% BeO. The targets were manufactured by Materion Electrofusion using a hot isostatic press. The rippled

patterns were formed via wire electrical discharge machining. The Be microstructure was imaged with the electron backscatter diffraction (EBSD) technique, Figure 4. The grain size distribution was calculated from the EBSD software, which designates the grains based on the local orientation, and tracks the grain size, Figure 5. The average grain size in the Be was 9.5 μm . EBSD scans indicate a weak (0001) basal plane texture orthogonal to the drive conditions, Figure 6. Nine Vickers hardness tests measured the average Be hardness to be 1832.86 MPa. The perturbation wavelength of the RT experiments is $\lambda = 4$ mm. The perturbation peak-to-valley amplitude for four experiments with 2 mm substrates is 0.48 mm. For the other two experiments, the perturbation amplitude is 0.38 mm and the targets are 1.78 mm thick. A sample machined Be target is shown in Figure 3. Bevels were machined into the outer edge of the targets to enable visualization of the ripple growth as the target accelerates and deforms. Without these bevels the outer edge of the target would hide the perturbation growth from a side-on view of the target.

We performed several Split-Hopkinson pressure bar (SHPB) experiments to characterize the dynamic behavior of the Be samples in lower strain-rates regimes and to compare with models calibrated via previous data.³⁴ The targets were made from the same batch of pressed S200F as the RT targets and the SPHB tests were conducted at LLNL. The SPHB experiments usually end with low strain in the sample due to brittle failure. Figure 7 shows the stress-strain curve for an experiment with a strain-rate of 2000 s^{-1} (the data from a single experiment is shown for illustration purposes and the SPHB experimental data for all the experiments is available in MIDAS³⁴). The strength models based on previous SHPB results seem accurately to describe the stress-strain response at these low strain-rates. It is not possible to discriminate among the different models in these regimes. The multiple parameter sets for the PTW model all fit the SHPB data but they predict different behavior for the higher strain-rates and pressures observed in the RT experiments, Figure 7b. The lack of differences in the models at these low strain-rates, and strains, and their significant divergence at high strain, strain rates, and pressures observed in many aerospace and defense applications is the main motivation for performing these strength experiments.³ The RT experiments we designed aim to provide data in these regimes to discriminate among the different available strength models.

B. Diagnostic Techniques

Two diagnostic techniques were used to capture the experimental data. X-ray radiographs at the Eridan-3 facility at RFNC-VNIIEF imaged the target perturbation growth, Figure 8. A 1 MeV, 0.15 μs pulse flash x-ray was used to record one image for each experiment, which was captured on a ADC-CR photochromatic screen.³⁵ Measurements of the free surface velocity of the targets were performed with a Velocity Interferometer System for Any Reflector (VISAR) during each experiment.³⁶ The pressure of the explosives on the loaded surface of the target determines the free surface velocity of the

target, and hence the expected RT growth. Comparing the VISAR data with simulations indicates that the drive conditions in the simulations match that of the experiments so a proper interpretation of the growth data can be made.

C. Experimental Results

We performed a total of six HE driven Be RT experiments. The radiographs are shown in Figure 9. The clear white region in the center of the radiograph is the Be liner. The bright area on the bottom of the radiograph is the HE and the bevels observed on the side are the Plexiglas brackets holding the liner. The absence of visible separation in the Be suggests that the targets do not spall, though this is not necessarily dispositive of no damage occurring during the experiment. The perturbations exhibit the characteristic RT mushroom shape at later times, Figure 9e and f. The time evolution of the perturbation growth was measured using the six radiographs and the growth factors are shown in Figure 10.

Measurements of the free surface velocity during each of the experiments indicate consistent drive conditions, Figure 11. Time $t = 0$ is the HE arrival time at the Be/HE interface. The flattening of the VISAR signal visible in most of the experiments around $0.7\mu\text{s}$ is probably due to signal loss. Most likely, the growth is so large that the perturbations consume the entire thickness of the target and distort the back of the target, deflecting the VISAR signal out of view.

III. Numerical Simulations of the Experiments

To model the experiments numerically, we used the Ares code, an Arbitrary Lagrangian Eulerian hydrodynamics code.³⁷ In Ares, scalar quantities such as density and internal energy are defined at cell centers while vector quantities like velocities are located at the cell vertices. These quantities are allowed to advance with the mesh during a Lagrange time step. The mesh is then relaxed subject to user-defined prescriptions and the scalar and vector quantities are remapped to the relaxed mesh. The problem is evolved temporally using a second order predictor-corrector scheme and spatially discretized using second order differences. The mesh resolution for all the simulations is $8\mu\text{m}$, at which point the simulation results are converged. We assumed planar symmetry and performed two-dimensional simulations of half wavelength slice of the system, thereby neglecting the release at the edges of the system.

The simulated system consists of the iron impactor, the HE, the vacuum gap, and a half wavelength ripple on the Be target. The iron impactor initiates the HE detonation, with its impact velocity determining the peak pressure in the HE explosion. The HE was modeled with a JWL++ reactive flow equation of state³⁸ using the parameters in Table 1. All other

materials used a tabulated equation of state from the LEOS data library based on a QEOS-like model.³⁹ We also compare the results using an analytic Gruneisen EOS. The drive, Figure 12a, and the growth, Figure 12b, are very similar regardless of the form of the equation of state.

Table 1: JWL++ reactive flow equation of state parameters for the HE

ρ_0 (g/cm ³)	A (Mb)	B (Mb)	R_1	R_2	ω	E_0 (Mb)	n	κ	G	b	β
1.89	7.8	3.9	0.1	1.2	0.3	0.159	7.4	7.8	3000	1	3.6

We examined the behavior of several of strength models, which typically have very different dependencies on strain, strain-rate, and shear modulus, as they relate to the Be yield stress. The Steinberg-Cochran-Guinan⁴⁰ (SCG) model is rate-independent but assumes “high” rates of order 10^5 s^{-1} . The shear modulus includes a linear pressure hardening term. The yield stress goes as the strain to the n th power, where n is a work hardening parameter, and also includes a linear pressure and thermal term. The Steinberg-Lund⁴¹ (SL) model is based on the SCG model and adds an additional strain-rate dependence in the thermal activation regime. The strain-rate depends on the inverse of the sum of an exponential of the thermal component of the stress with the inverse of the thermal component of the stress. The Preston-Tonks-Wallace⁴² (PTW) model describes material behavior in both the thermal activation and phonon drag regimes over many orders of magnitude of strain-rate. At low strain-rates ($<10^4 \text{ s}^{-1}$), two different expressions for the work hardened saturation stress and yield stress are used to describe the thermal regime and vary as the error function of the logarithm of the inverse of the strain rate. At high strain-rates, the phonon drag regime for dislocation motion is described using the theory of overdriven where the saturation stress and yield stress are set equal and are related to a power of the strain-rate divided by the atomic vibration frequency. The stress in the transition region between the low and high strain-rate regimes is the maximum of the low and high strain-rate regime stresses. A single model can have different parameter sets to describe a given material. In this paper, we use four versions of the PTW model, each differing in their model parameters: the original parameters⁴², and others proposed by Blumenthal, Chen, and Preston⁴³, shown for Be in Table 2. The Relaxation Model of Beryllium Strength⁴⁴ (RING) model includes relaxation terms, twinning effects, and annealing effects. Finally, the Mechanical Threshold Stress⁴⁵ model, valid at low strain-rates, includes thermal activation and dislocation effects. The stress is linear combination of different stresses caused by dislocation barriers. These are scaled via factors representing the structure functions for the various dislocation barriers. The scaling factors are highly non-linear functions of temperature and strain-rate. These models have been calibrated to data from low pressures and low strain and strain-rate experiments. Predicting the RT growth in higher pressure and strain-rate regimes is therefore particularly challenging.

Table 2: Summary of the different PTW Be material parameters used in this paper (see Ref⁴² for the parameter definitions)

	Original PTW	Chen's PTW (PTWC)	Preston's PTW (PTWP)	Blumenthal's PTW (PTWB)
θ	0.04	0.025	0.045	0.0394
p	1.4	2	2.5	2
s_0	0.007	0.0093	0.00845	0.0077
s_∞	0.0012	0.00135	0.00083	0.0006
κ	0.14	0.11	0.12	0.145
γ	1E-05	1E-05	7E-05	1E-06
y_0	0.0015	0.0009	0.00129	0.0018
y_∞	0.0005	0.0009	0.00051	0.0004
y_1	0.007	0.0093	0.00845	0.0077
y_2	0.25	0.16	0.16	0.4
β	0.25	0.16	0.16	0.25

By tuning the velocity of the iron impactor detonating the second stage HE, Figure 2, we ensure that the simulations have the same drive conditions as the experiments. Comparisons between the velocimetry data of the Be targets measured by VISAR and a simulation using the PTW model are presented in Figure 11. Simulations with different strength models do not present significantly different predictions of the free surface velocity because the drive conditions are essentially independent of the strength models. The simulations are sufficient to allow for an interpretation of the growth data with an adequate acceleration profile.

Simulations of the experiment indicate that the Be target reaches 50 GPa and strain-rates of 10^6 s^{-1} , the phase-space where the model predictions of the perturbation growth differ. We present pseudo-color plots of pressure and strain-rate in Figure 13. Initially, a compression wave induced by the iron impactor travels through the HE, thereby detonating it, Figure 13a. The HE then expands through the vacuum gap and loads against the Be target, Figure 13b. The target reaches 50 GPa peak pressure and strain-rates of 10^6 s^{-1} , Figure 13c. The ripples at the HE-Be interface grow as the target is accelerated by the expanding HE gas, Figure 13d and e.

Figure 10 also presents a comparison between the predicted growth factors of the perturbations using different strength models and the experimental data points as a function of target displacement. The data suggest that the Be ripples grew close to classically and are consistent with low strength in the Be. “Classically” usually refers to a constant acceleration at a non-viscous liquid/gas interface. In this context we use it to describe growth in the presence of no strength or viscosity regardless

of the dynamic loading profile. From the radiographs, we observe that the ripples have a significant mushroom shape, indicative of a classical RT growth in the non-linear regime. Consequently, most of the strength models underpredict the growth of the perturbations. The MTS model predicts very little growth, which indicates that the work hardening is overpredicted for this region of the phase space. The MTS stress-strain curve as shown in Figure 1 clearly illustrates this as it is steeper than the other stress-strain curves in this region of phase space. The RING model, as adopted in Ares, is the strength model closest to the experimental data. The experiments enable us to eliminate several models, such as the MTS model, which do not capture the data in this regime. The results indicate that the RING and SCG models are adequate in this regime. The small difference among the PTW models are not as significant as the differences between the PTW and the other models in general. The data indicate that the models in general are inadequate for capturing the high strain, strain-rate, pressure regime of the experiments. These models require better physics-based components to underwrite their validity. This is due in part because they are based on observations made in different parts of the phase space and they cannot be reliably extrapolated into other regions.

IV. Recovery Experiments

Current plasticity models generally assume deformation mechanisms driven by dislocations. However, Be is known to incur substantial twinning and can experience brittle failure under room temperature conditions. Previous work¹⁵ on hot isostatically pressed S200F indicates that at strains up to ~20% under uniaxial compression the dominant deformation mechanism is basal slip with the contribution from twins peaking at 10% strain but never becoming dominant. To understand the extent of twinning and failure that might be present in higher strain-rate regimes such as our RT experiments, we also performed Be recovery experiments, where Be samples were loaded and then recovered for analysis. The goal of these experiments was to explore the effect of loading and shock strength on the Be microstructure and to determine Be dislocation dynamics. Unfortunately it is not possible to recover the RT targets themselves since their thin nature causes them to essentially disintegrate at late times before they can be recovered. As such, thicker targets were used with different loading profiles from the RT experiments making an exact comparison of the deformation impossible; nonetheless, the path we chose is enough to describe the behavior of Be under uniaxial loading and at least similar drive conditions.

We performed two types of recovery experiments. In the first, a Be target of 60x15mm was sandwiched between two layers of aluminum (120x0.5mm for the front disk and 120x5mm for the back disk) and placed near a charge of HE. The Be sample experienced quasi-isentropic loading resulting from the detonation of the HE. The compression wave steepened to

a shock as it traveled in the Be. This experiment was designed to keep the pressure in the material constant, but to have a varying strain-rate (from 10^5 to 10^{10} s^{-1}). In the second experiment, a Be sample of the same dimensions was also placed between two layers of aluminum, but this time an HE charge launched an aluminum impactor ($\varnothing 120 \times 2 \text{ mm}$) resulting in a shock wave that decreased in strength as it traveled in the Be. In this case, the strain-rate was constant (approximately 10^5 s^{-1}) but the pressure varied from 15 to 10 GPa. Manganin-based pressure sensors (MPS) were used to measure the pressure in the sample. Given the reputation of brittle failure in Be and uncertainty in the dominant deformation mechanism *a priori* expectations from the experiments ranged from mild deformation to complete disintegration.

A microsection of the recovered Be sample for the first type of experiment is shown in Figure 14. The pressure sensors indicated a peak pressure of 25 GPa in the sample. The microsection reveals a fine-grained structure with an average grain size of $14 \pm 6.7 \text{ }\mu\text{m}$. A crack is clearly visible. The observed twinning fraction was less than fifty percent. A recovered sample from the second type of experiment illustrates the partial destruction of the Be sample under this type of loading, Figure 15. In this case, the peak pressure in the sample was around 14 GPa. From these two types of recovery experiments it is clear that the samples fractured but did not completely disintegrate.

Using the MPS data we calibrated the simulations to obtain the same conditions as in the experiments, Figure 16. The different loading paths and target strains are clearly visible when comparing Figure 17 and Figure 18. In the first experiment, the simulation indicates that the pressure inside the target reached 26 GPa and remained constant throughout the material for about $1 \text{ }\mu\text{s}$ before decreasing smoothly. The strain inside the target reached 0.1, remained constant, and then increased again. In the second experiment, the pressure at the leading edge of the Be target increased rapidly to approximately 15 GPa and decreased sharply thereafter to a near-constant value of 10 GPa. The amplitude of the shock wave decreased as it traveled in the Be. The strain varied from 0.15 to 0.11 depending on the depth in the Be target. The simulations also indicate different strain-rate behaviors in the two experiments, Figure 19. In the first experiment, an initial spike in strain-rate is followed by a constant rate of $\sim 2 \times 10^4 \text{ s}^{-1}$. In the second experiment, the strain-rate is around 10^5 s^{-1} for about $0.25 \text{ }\mu\text{s}$ and then decreases rapidly to approximately $2 \times 10^3 \text{ s}^{-1}$.

V. Conclusion

We performed six HE-driven Be RT experiments to discriminate among different strength models. These experiments were designed to reach a phase space where the models' growth predictions differed. The data suggest that the Be ripples growth was only slightly mitigated by strength indicating weaker than predicted behavior. The RING model does reasonably

well predicting the growth for the larger initial amplitude experiments. The other models underpredict the perturbation growth. The experimental results challenge the underlying assumptions of the existing strength models. Once the material enters a phase space in strain, strain-rate and pressure away from the calibration regimes of the current models its predicted behavior breaks down. In part the models rely on a limited range of data, but also limited physical assumptions, mostly having to do with using strain (as a surrogate for “dislocation” interaction) and strain rate as the manifestations to plastic flow. However, as shown in the recovery experiments, that while the twinning fraction was less than 50%, it cannot be overlooked as an important physical mechanism in the material flow. Additionally, while the RT experiments show no indication of spall or other failure (e.g., cracks), the recovery experiments do. The loading profiles between the two experiments differ and the recovery experiments by their nature are done late in time; however, the recovery experiments do suggest failure mechanisms should be included in any advanced Be plasticity model. If similar experiments are proposed for future work we recommend adjusting the existing models to match the data set presented here and then driving the targets through different strain states by adjusting the initial perturbations, and hence, the growth rate and strain. Varying the initial perturbations wavelength would lead to a dispersion curve that could increase our understanding of Be strength in these extreme regimes. Higher temperature experiments could also be a means to distinguish the models in future experiments.

Acknowledgements

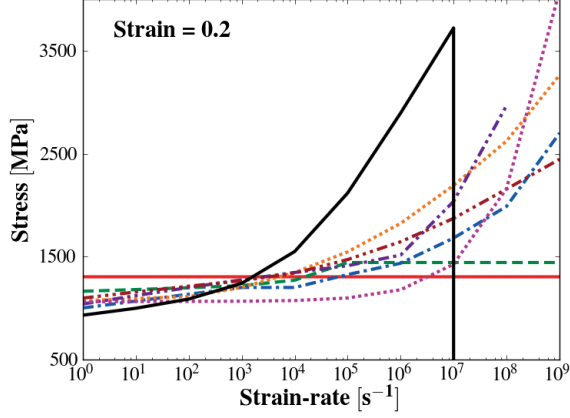
The authors would like to acknowledge the support of Gil Gallegos, Jeff Florando, Mary LeBlanc, Bassem El-dasher and Dione Archeta for their support in the procurement and characterization of the targets fired in these experiments. They would also like to express their gratitude to William Fritchie and Todd Stephens for help in navigating the export control maze so that these targets could be delivered to RFNC-VNIIEF. They also wish to thank Shou-Rong Chen for allowing us to share the updated Los Alamos PTW parameters for Be. This work was performed under the auspices of the U.S. Department of Energy by Lawrence Livermore National Laboratory under Contract DE-AC52-07NA27344. Work at RFNC-VNIIEF was supported in part by Contract B590737 between LLNL and RFNC-VNIIEF.

Bibliography

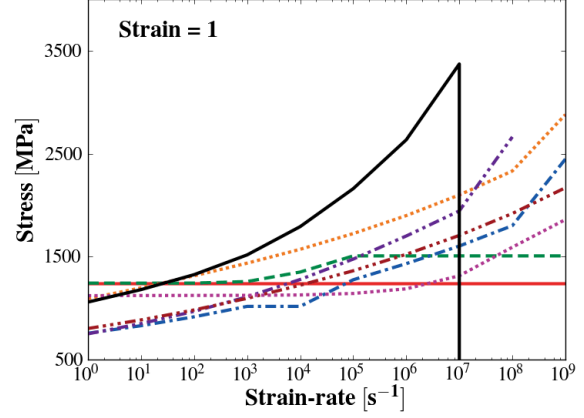
- ¹ W.R. Blumenthal, S.P. Abeln, D.D. Cannon, G.T. Gray, and R.W. Carpenter, in *AIP Conf. Proc.* (AIP, 1998), pp. 411–414.
- ² T. a. Sisneros, D.W. Brown, B. Clausen, D.C. Donati, S. Kabra, W.R. Blumenthal, and S.C. Vogel, *Mater. Sci. Eng. A* **527**, 5181 (2010).
- ³ J.M. Marder, *J. Mater. Energy Syst.* **8**, 17 (1986).

- ⁴ F. Ayer, *Materials for Space Optics, Generic Requirements* (Daytona Beach, Florida, 1984).
- ⁵ K. Bennett, R. Varma, and R. Von Dreele, *Scr. Mater.* **40**, 825 (1999).
- ⁶ L.B. Norwood, *J. Spacecr. Rockets* **22**, 560 (1985).
- ⁷ S.P. Abeln and P. Kyed, *Summary of Beryllium Specifications: Current and Historical* (Golden, Colorado, 1990).
- ⁸ U.S. Lindholm and L.M. Yeakley, *Effect of Strain Rate, Temperature and Multiaxial Stress on the Strength and Ductility of S-200E Beryllium and 6Al-4V Titanium* (San Antonio, TX, 1972).
- ⁹ D.R. CHRISTMAN and N.H. FROULA, *AIAA J.* **8**, 477 (1970).
- ¹⁰ D.R. Christman and F.J. Feistmann, *Dynamic Properties of S-200-E Beryllium* (Warren, MI, 1972).
- ¹¹ U.S. Lindholm, L.M. Yeakley, and D.L. Davidson, *Biaxial Strength Tests on Beryllium and Titanium Alloys* (San Antonio, TX, 1974).
- ¹² L.E. Pope and J.N. Johnson, *J. Appl. Phys.* **46**, 720 (1975).
- ¹³ S. Jönsson and J. Beuers, *Mater. Sci. Eng.* **91**, 111 (1987).
- ¹⁴ J.W. Christian and S. Mahajan, *Prog. Mater. Sci.* **39**, 1 (1995).
- ¹⁵ W.R. Blumenthal, in *AIP Conf. Proc.* (AIP, 2004), pp. 525–528.
- ¹⁶ D.W. Brown, B. Clausen, T.A. Sisneros, L. Balogh, and I.J. Beyerlein, *Metall. Mater. Trans. A* **44**, 5665 (2013).
- ¹⁷ D.W. Brown, S.P. Abeln, W.R. Blumenthal, M.A.M. Bourke, M.C. Mataya, and C.N. Tomé, *Metall. Mater. Trans. A* **36**, 929 (2005).
- ¹⁸ D.W. Brown, S.R. Agnew, S.P. Abeln, W.R. Blumenthal, M. a. M. Bourke, M.C. Mataya, C.N. Tomé, and S.C. Vogel, *Mater. Sci. Forum* **495-497**, 1037 (2005).
- ¹⁹ D.W. Brown, J.D. Almer, B. Clausen, P.L. Mosbrucker, T.A. Sisneros, and S.C. Vogel, *Mater. Sci. Eng. A* **559**, 29 (2013).
- ²⁰ V. Skokov, V. Arinin, D. Kryuchkov, V. Ogorodnikov, V. Raevsky, K. Panov, V. Peshkov, and O. Tyupanova, in *AIP Conf. Proc.* (2012), pp. 1073–1076.
- ²¹ C.D. Adams, W.W. Anderson, G.T. Gray, W.R. Blumenthal, C.T. Owens, F.J. Freibert, J.M. Montoya, P.J. Contreras, M. Elert, M.D. Furnish, W.G. Proud, and W.T. Butler, in *AIP Conf. Proc.* (2009), pp. 509–512.
- ²² C.D. Adams, W.W. Anderson, W.R. Blumenthal, and G.T. Gray, *J. Phys. Conf. Ser.* **500**, 112001 (2014).
- ²³ Y.I. Mescheryakov, A.K. Divakov, Y.A. Petrov, and C.F. Cline, *Int. J. Impact Eng.* **30**, 17 (2004).
- ²⁴ Y.I. Mescheryakov, A.K. Divakov, and N.I. Zhigacheva, *Int. J. Solids Struct.* **41**, 2349 (2004).
- ²⁵ C.M. Cady, C.D. Adams, L.M. Hull, G.T. Gray, M.B. Prime, F.L. Addessio, T.A. Wynn, P.A. Papin, and E.N. Brown, *EPJ Web Conf.* **26**, 01009 (2012).
- ²⁶ E.N. Brown, C.M. Cady, G.T. Gray, L.M. Hull, J.H. Cooley, C. a Bronkhorst, and F.L. Addessio, *J. Phys. Conf. Ser.* **500**, 112013 (2014).

- ²⁷ M.L. Wilkins and M.W. Guinan, J. Appl. Phys. **44**, 1200 (1973).
- ²⁸ L. Rayleigh, Proc. R. Soc. A Math. Phys. Eng. Sci. **84**, 247 (1910).
- ²⁹ G. Taylor, Proc. R. Soc. A Math. Phys. Eng. Sci. **201**, 192 (1950).
- ³⁰ J.W. Miles, (unpublished) (1966).
- ³¹ J.F. Barnes, P.J. Blewett, R.G. McQueen, K. a. Meyer, and D. Venable, J. Appl. Phys. **45**, 727 (1974).
- ³² J.H. Cooley, R.T. Olson, and D. Oro, J. Phys. Conf. Ser. **500**, 152003 (2014).
- ³³ V.A. Raevsky, *Influence of Dynamic Material Properties on Perturbation Growth in Solids* (Sarov, 2009).
- ³⁴ M. Tang, P.D. Norquist, J.N. Barton, N.R., Durrenberger, J. K., Florando, and A. Attia, *MIDAS: A Comprehensive Resource of Material Properties* (2010).
- ³⁵ V. a. Arinin and B.I. Tkachenko, Pattern Recognit. Image Anal. **19**, 63 (2009).
- ³⁶ C.F. McMillan, D.R. Goosman, N.L. Parker, L.L. Steinmetz, H.H. Chau, T. Huen, R.K. Whipkey, and S.J. Perry, Rev. Sci. Instrum. **59**, 1 (1988).
- ³⁷ G. Bazan, in *Proc. from 2nd Int. Work. Lab. Astrophys. with Intense Lasers*, edited by B.A. Remington (Lawrence Livermore National Laboratory, Livermore, CA, 1998).
- ³⁸ P.C. Souers, S. Anderson, J. Mercer, E. McGuire, and P. Vitello, Propellants, Explos. Pyrotech. **25**, 54 (2000).
- ³⁹ R.M. More, K.H. Warren, D. a. Young, and G.B. Zimmerman, Phys. Fluids **31**, 3059 (1988).
- ⁴⁰ D.J. Steinberg, S.G. Cochran, and M.W. Guinan, J. Appl. Phys. **51**, 1498 (1980).
- ⁴¹ D.J. Steinberg and C.M. Lund, J. Appl. Phys. **65**, 1528 (1989).
- ⁴² D.L. Preston, D.L. Tonks, and D.C. Wallace, J. Appl. Phys. **93**, 211 (2003).
- ⁴³ M.B. Prime, S.-R. Chen, and C. Adams, in *AIP Conf. Proc.* (2012), pp. 1035–1038.
- ⁴⁴ V.A. Raevsky, O.N. Aprelkov, O.N. Ignatova, V.I. Igonin, A.I. Lebedev, S.S. Nadezhin, M. a. Zocher, D. Preston, and A. Coul, EPJ Web Conf. **10**, 00022 (2011).
- ⁴⁵ P.S. Follansbee and U.F. Kocks, Acta Metall. **36**, 81 (1988).



a) Strain = 0.2.



b) Strain = 1.

Figure 1: Total stress as a function of strain-rate in Be for different strength models (curves determined by setting the model parameters in MIDAS³⁴ for adiabatic uniaxial compression at 300K and 0 initial pressure). Left (a): strain = 0.2; right (b): strain = 1. Solid red: SCG; dashed green: SL; dot-dashed blue: PTW; dotted orange: PTWP; dot-dot-dashed purple: PTWC; dot-dot-dot-dashed burgundy: PTWB; dotted magenta: RING; solid black: MTS. The models and different flavors of models are detailed in Section II A.

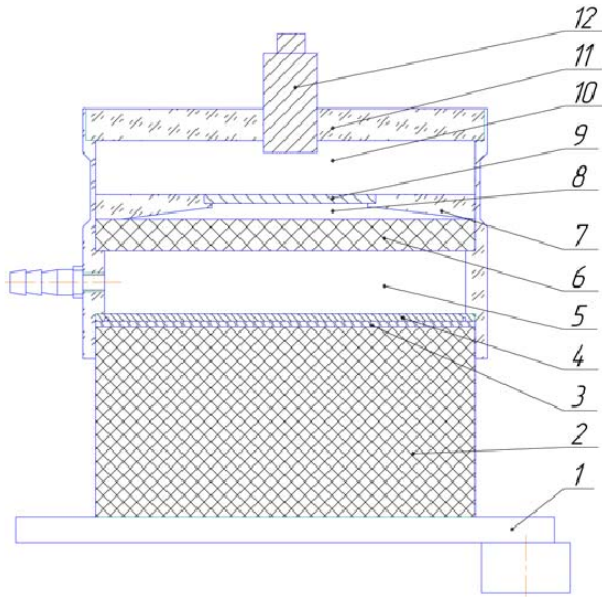
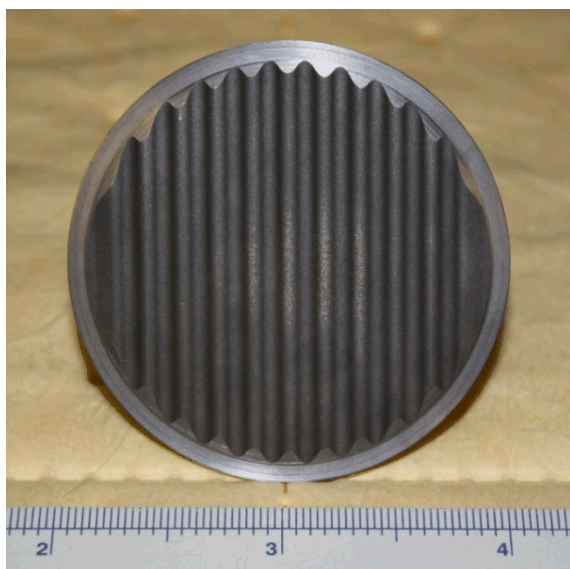
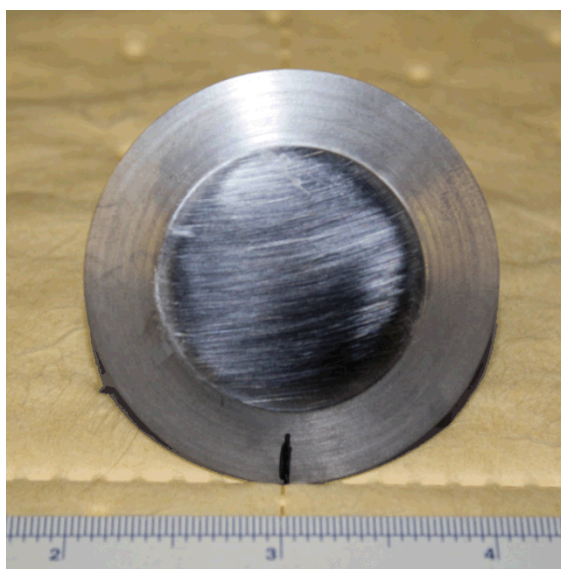


Figure 2: Two stage loading device for the quasi-isentropic loading of a rippled Be target. Planar shock wave generator (1); first stage HE (2, $\varnothing 90\text{mm} \times 80\text{mm}$); plexiglass damper (3, $\varnothing 90\text{mm} \times 2\text{mm}$); Iron impactor (4, $\varnothing 90\text{mm} \times 2.2\text{mm}$); vacuum gap (5, 10mm); second stage HE (6, $\varnothing 90\text{mm} \times 10\text{mm}$); plexiglass bracket (7); vacuum gap (8, 2mm); Be target (9, $\varnothing 50\text{mm}$); vacuum volume (10); plexiglass disk (11, $\varnothing 90\text{mm} \times 10\text{mm}$); optical gauge (12).



a) Front view (loading side).



b) Back view (free surface).

Figure 3: Pictures of a machined Be target. The graduated ruler is in cm. Left (a): front view; right (b): back view.

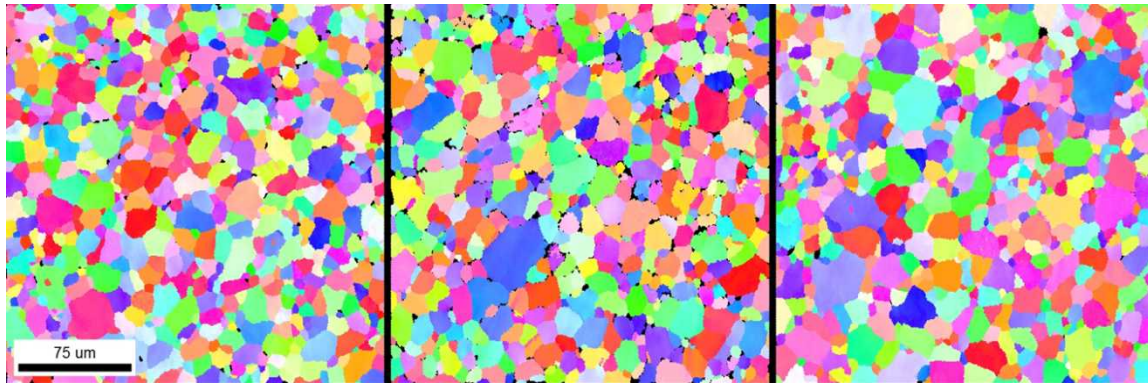


Figure 4: Be microstructure from three EBSD scans of 250 x 250 μm . The colors are used to enhance visualization of the grains.

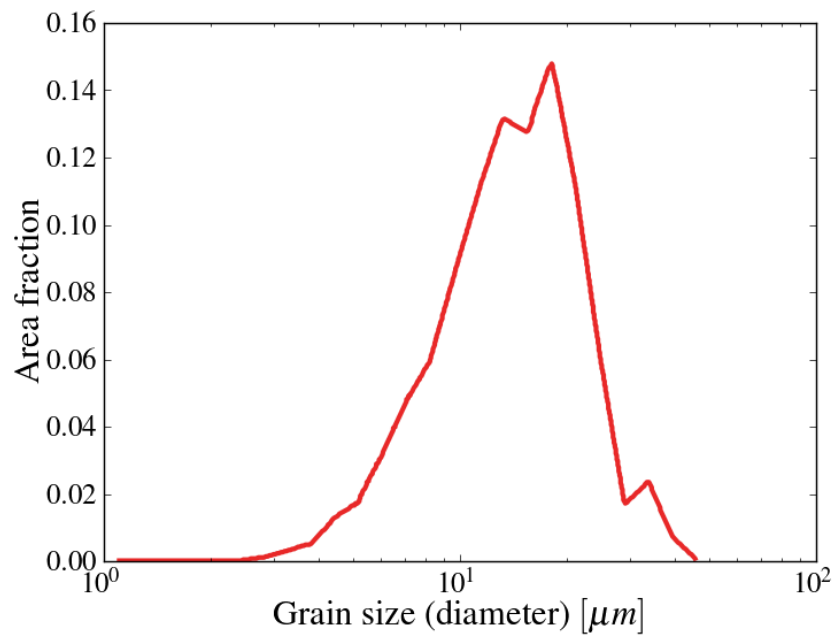


Figure 5: Grain size distribution from EBSD scans. 2038 grains were measured and the average grain size is 9.5 μm .

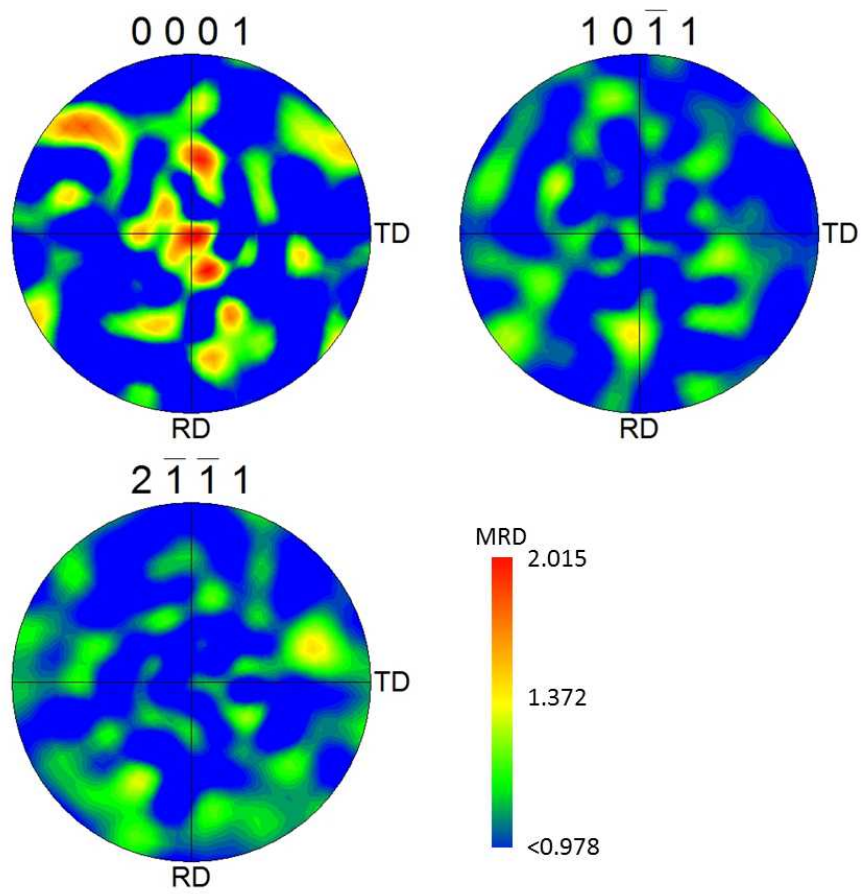
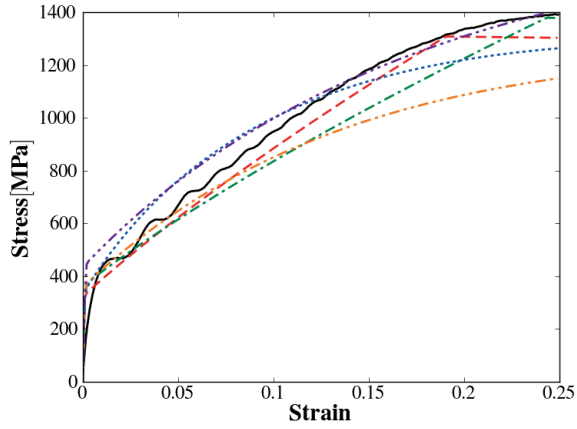
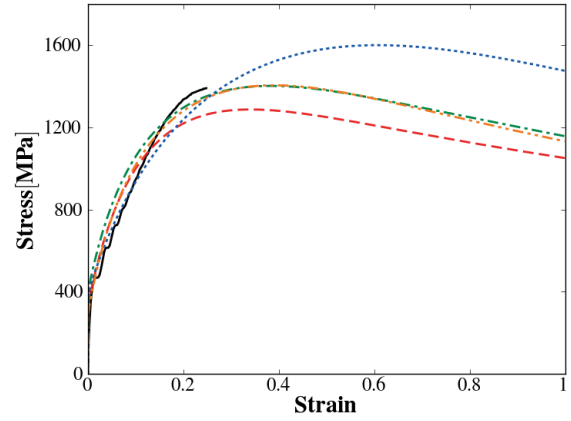


Figure 6: Polar maps of grain orientation from EBSD scans. Color map is in units of multiples of a random density (MRD) with a max = 2.015 and min = 0.978. TD is the transverse direction and RD the rolling direction.



a) Solid black: SPHB experimental data at ambient temperature; dashed red: SCG; dot-dashed green: SL; dotted blue: PTW; dot-dot-dashed orange: RING; dot-dot-dot-dashed purple: MTS.



b) Solid black: SPHB experimental data at ambient temperature; dashed red: PTW; dot-dashed green: PTWC; dotted blue: PTWP; dot-dot-dashed orange: PTWB.

Figure 7: Stress as a function of strain in Be for a characteristic strain-rate of 2000 s^{-1} . Left (a): comparing to the SCG, SL, PTW, RING, and MTS models; right (b): comparing four different PTW parameter sets over a large range of strains.

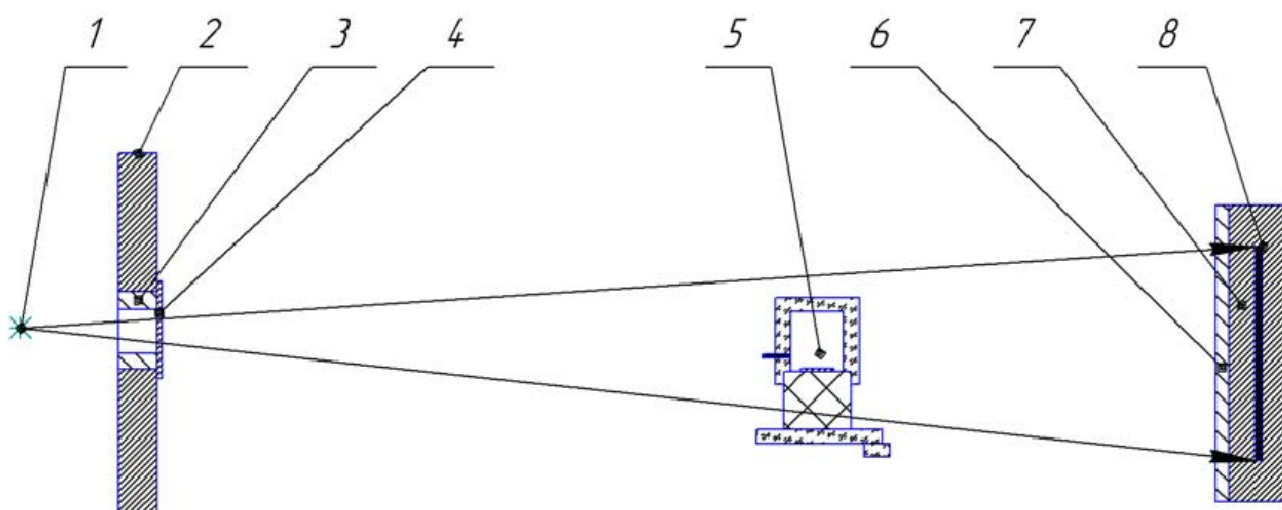


Figure 8: X-ray radiograph diagnostic setup. X-ray source (1); armored protection (2); collimator (3); protective screen (4); experimental assembly (5); protective setup (6); armored cassette (7); ADC-CR screen (8).

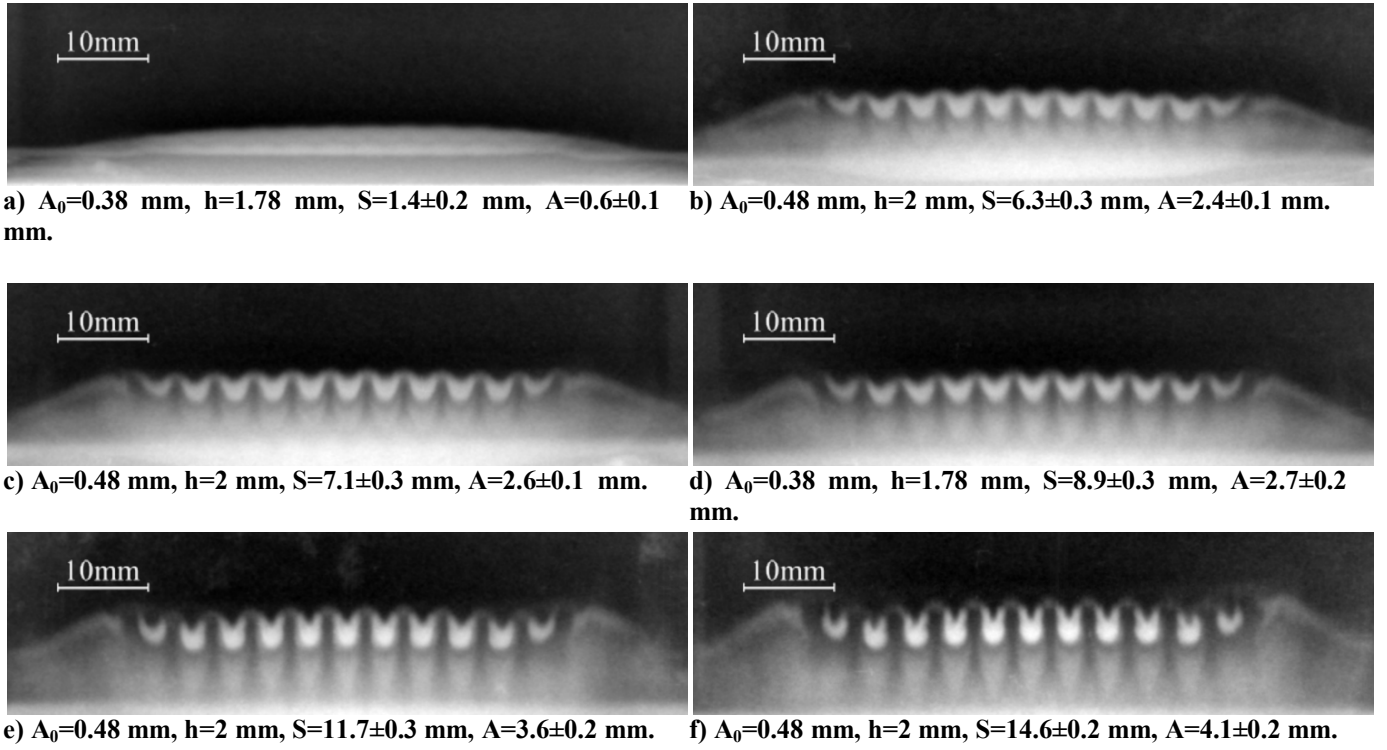
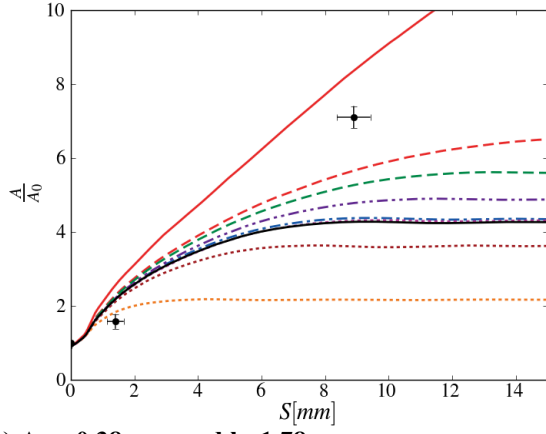
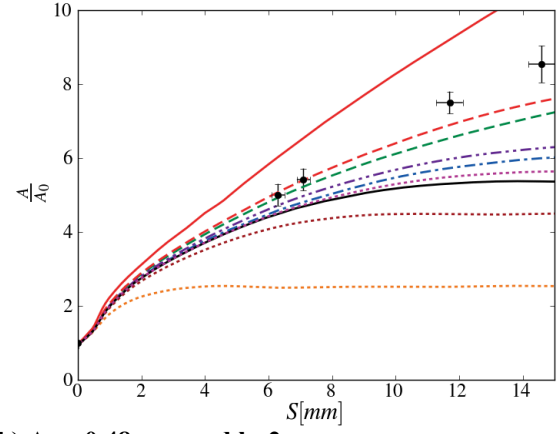


Figure 9: Radiographs of the six HE driven Be RT experiments. The brighter area on the bottom of the radiograph is the HE. The clear white region in the center of the radiograph is the Be liner. A_0 is the initial peak-to-valley perturbation amplitude, h is the initial target thickness, S is the target displacement and A is the measured peak-to-valley perturbation amplitude. The direction of motion is towards the top of the images.



a) $A_0 = 0.38$ mm and $h=1.78$ mm.



b) $A_0 = 0.48$ mm and $h=2$ mm.

Figure 10: Growth factors as a function of displacement. Left (a): $A_0 = 0.38$ mm and $h=1.78$ mm; right (b): $A_0 = 0.48$ mm and $h=2$ mm. Black dots: experimental data; solid red: no strength; dashed green: SCG; dot-dashed blue: SL; dotted orange: MTS; dot-dot-dashed purple: PTW; solid black: PTW (Chen); dotted maroon: PTW (Preston); dotted magenta: PTW (Blumenthal); dashed red: RING.

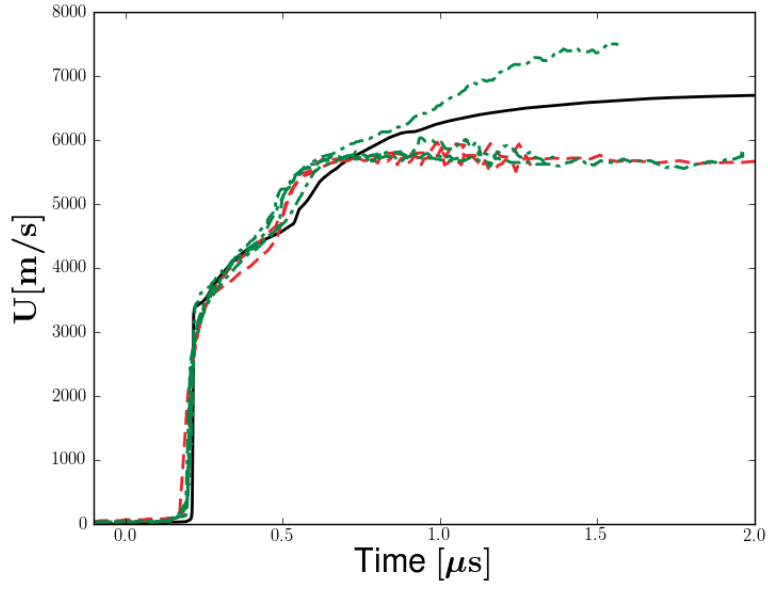


Figure 11: Free surface velocity, U , as a function of time. $t=0$ is the HE arrival time at the Be/HE interface. Dashed red: $h=1.78$ mm; Dash-dotted green: $h=2$ mm; black: numerical simulation.

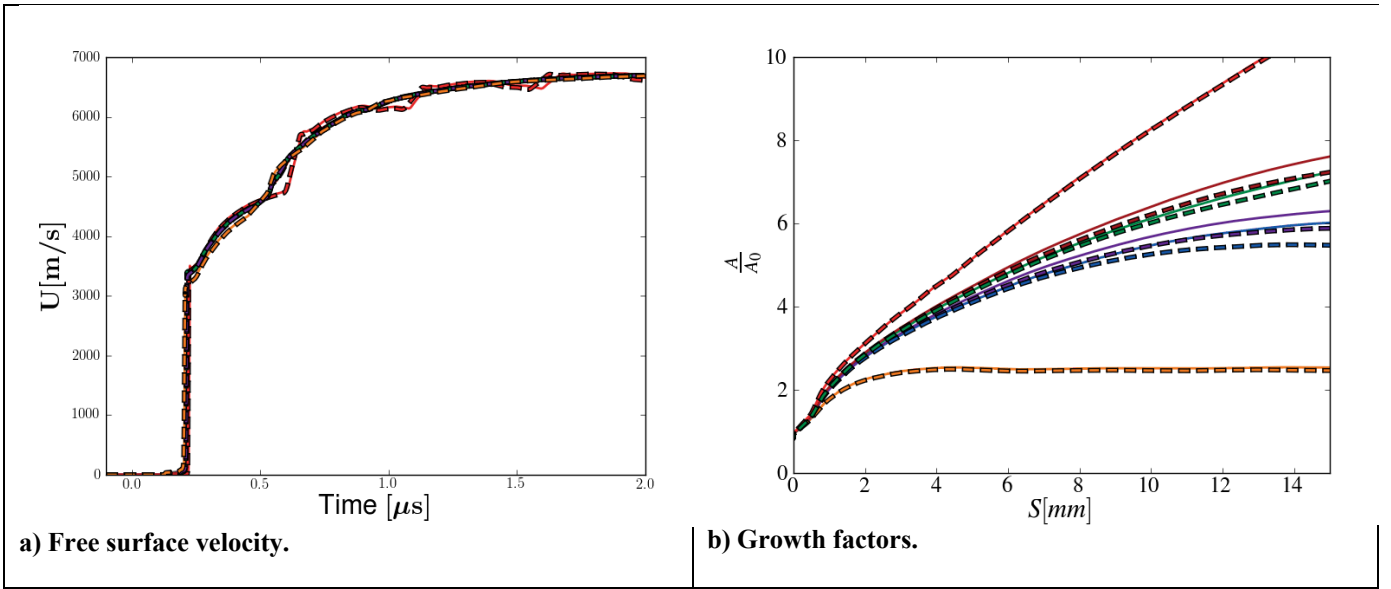
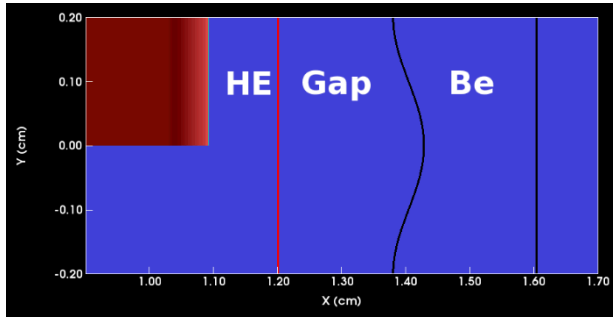
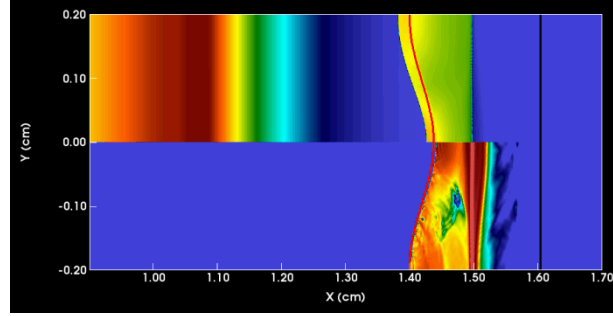
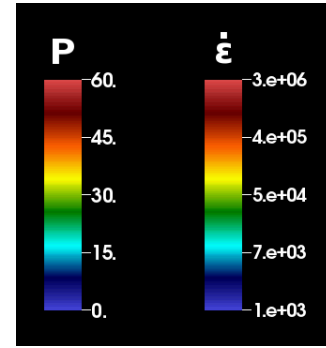


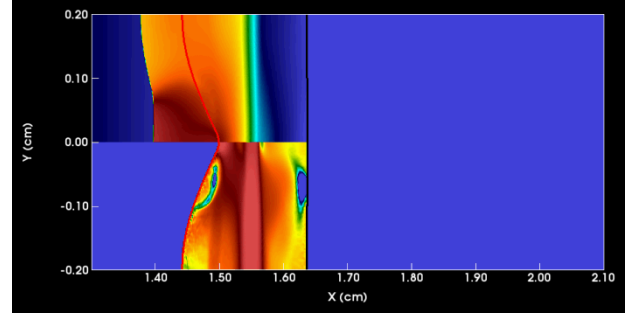
Figure 12: Simulation of a 2 mm thick target with $A_0=0.48$ mm. Left (a): free surface velocity as a function of time where $t=0$ is the HE arrival time at the Be/HE interface; right (b): growth factors as a function of time. Solid: tabulated equation of state from the LEOS data library; black outlined dashed: analytic Gruneisen equation of state. Red: no strength; green: SCG; blue: SL; purple: PTW; orange: MTS; maroon: RING.



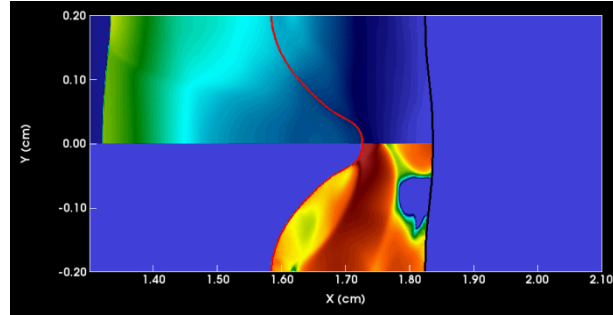
a) $t = -0.3 \mu\text{s}$.



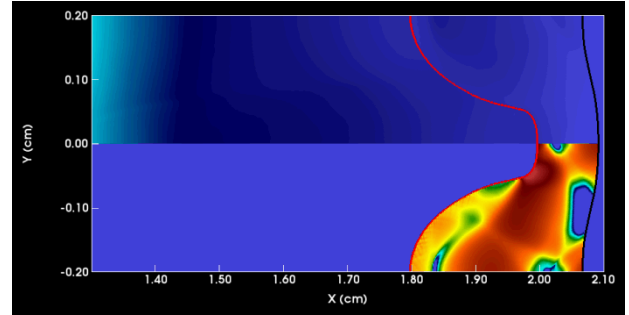
b) $t = 0.1 \mu\text{s}$.



c) $t = 0.3 \mu\text{s}$.



d) $t = 0.7 \mu\text{s}$.



e) $t = 1.1 \mu\text{s}$.

Figure 13: Pseudocolors of pressure (top half) and strain-rates (bottom half) in the HE and Be target. Red line: HE-Be interface; black line: Be back. $t=0$ is the HE arrival time at the Be/HE interface. Pressure color map is in units of GPa with $\min = 0$ GPa and $\max = 60$ GPa. Strain-rate colormap is in units of s^{-1} with $\min = 10^3 \text{ s}^{-1}$ and $\max = 3 \times 10^6 \text{ s}^{-1}$.

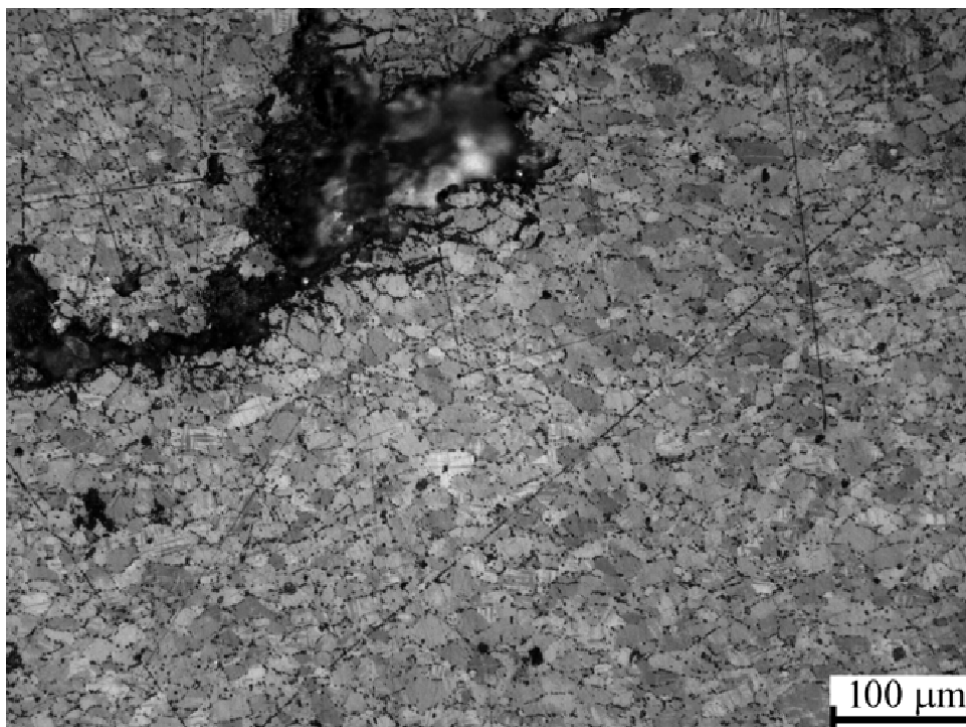


Figure 14: Microsection of Be sample loaded with a quasi-isentropic compression wave.



Figure 15: Picture of post-shot Be sample loaded with a thin metal impactor.

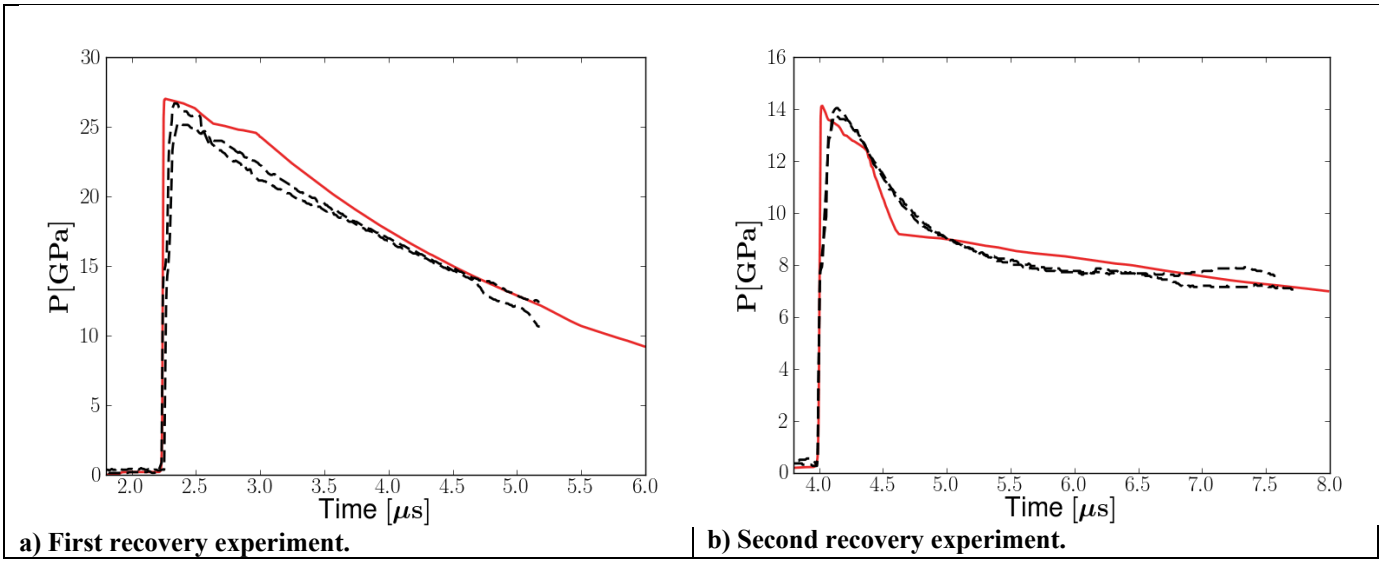


Figure 16: Pressure at the MPS locations as a function of time for the recovery experiments. $t = 0$ is the arrival time of the first pressure spike at the loaded surface of the Be. Left (a): for the first recovery experiment; right (b): for the second recovery experiment. Dashed black: experimental data from the MPS; solid red: simulation data.

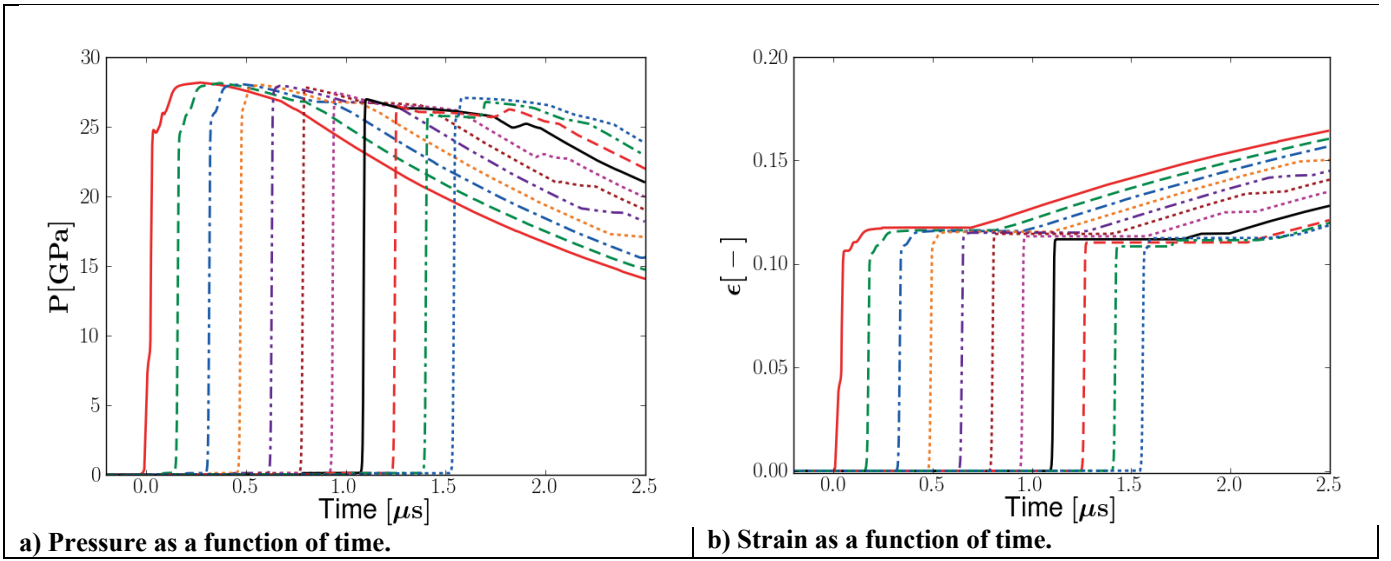


Figure 17: Pressure and strain for the first recovery experiment at various depths in the Be target. $t = 0$ is the arrival time of the first pressure spike at the loaded surface of the Be. Left (a): for the first recovery experiment; right (b): for the second recovery experiment. Solid red: 0.015 cm; dashed green: 0.15 cm; dot-dashed blue: 0.3 cm; dotted orange: 0.45 cm; dot-dot-dashed purple: 0.6 cm; solid black: 0.75 cm; dotted maroon: 0.9 cm; dotted magenta: 1.05 cm; dashed red: 1.2 cm; dot-dashed green: 1.35 cm; dashed blue: 1.485 cm.

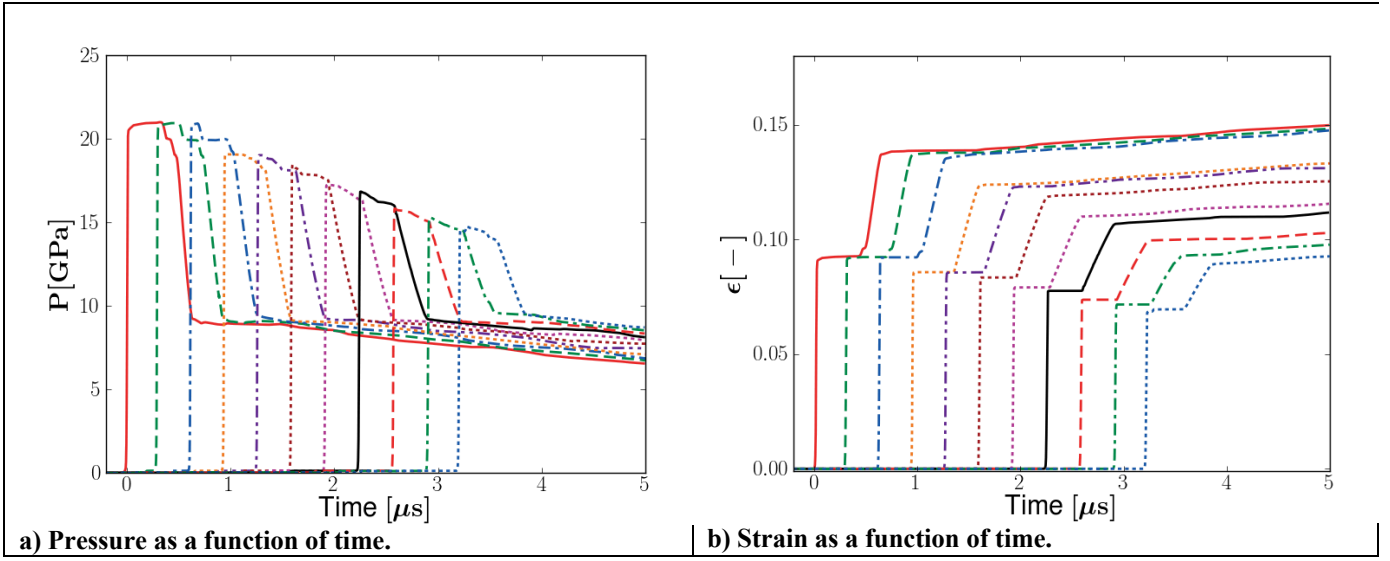


Figure 18: Pressure and strain for the second recovery experiment at various depths in the Be target. $t = 0$ is the arrival time of the first pressure spike at the loaded surface of the Be. Left (a): pressure as a function of time; right (b): strain as a function of time. Solid red: 0.015 cm; dashed green: 0.15 cm; dot-dashed blue: 0.3 cm; dotted orange: 0.45 cm; dot-dot-dashed purple: 0.6 cm; solid black: 0.75 cm; dotted maroon: 0.9 cm; dotted magenta: 1.05 cm; dashed red: 1.2 cm; dot-dashed green: 1.35 cm; dashed blue: 1.485 cm.

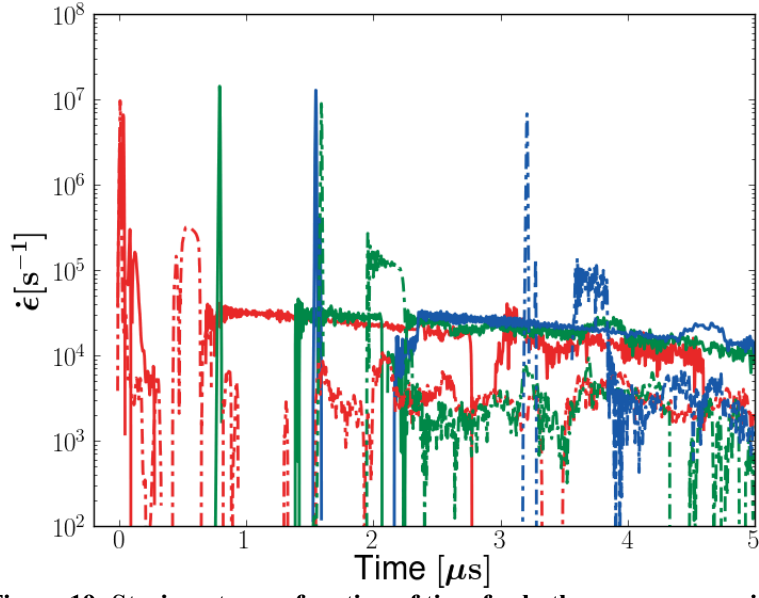


Figure 19: Strain-rate as a function of time for both recovery experiments at various depths in the Be target (red: leading edge; green: middle; blue: trailing edge). $t = 0$ is the arrival time of the first pressure spike at the loaded surface of the Be. Solid: first recovery experiment; dashed: second recovery experiment.